Second-order optical coherence tomography: deeper and turbulence-free imaging

Amir Nevet,* Tomer Michaeli, and Meir Orenstein

Department of Electrical Engineering, Technion, Haifa 32000, Israel
**Corresponding author: nevet@tx.technion.ac.il*

Received September 26, 2012; accepted November 12, 2012;
posted November 19, 2012 (Doc. ID 176986); published January 4, 2013

The superior resolution of optical coherence tomography (OCT) with respect to alternative imaging modalities makes it highly attractive, and some of its applications are already in extensive clinical use. However, one of the major limitations of OCT is that the tomographic picture it generates is depth-limited to approximately 1 mm in most biological tissues. This is mainly due to the spatially turbulent nature of the tissue, which leads to scattering. Moreover, this technique is extremely sensitive to temporal variations in the medium. We show that insensitivity to temporal and spatial turbulence may be gained by replacing the linear detector with an ultrasensitive two-photon detector. These results have striking implications on the attainable penetration depth of optical imaging and on its sensitivity to sample motion.

OCIS codes: 190.4180, 030.1640, 110.4500.

1. INTRODUCTION

Optical coherence tomography (OCT) is a unique three-dimensional imaging technique, providing a micrometer-scale resolution of scattering media to a depth of a few millimeters via a nondestructive, contact-free measurement [1]. This technique initially evolved as a method for determining the position and magnitude of reflection sites in integrated optics [2,3], but its exclusive advantages were soon after recognized as suitable for imaging of biological tissues [4]. Today, OCT is an invaluable tool in ophthalmology [5], shows great promise in intravascular imaging [6,7], and has a potential for future "optical biopsy" in dermatology [8] as well as for applications outside the field of biomedical imaging [9]. OCT is based on a Michelson interferometer incorporating the sample in one of its arms. The initial setups conducted time-domain measurements using a moving reference mirror; however, other variations based on frequency-domain measurements were later presented [10,11] and became widespread, benefiting from higher scan speed at the cost of decreased dynamic range [12] and higher sensitivity to sample movements [13]. Other variants of OCT include polarization-sensitive OCT (PS-OCT), which gives functional information regarding the biochemical composition where highly organized tissues are present [14]. The fundamental advantage of OCT over other imaging modalities is its high resolution, while its greatest disadvantage is its relatively poor penetration depth. The former is due to the employment of short-coherence-length optical sources, while the latter is mainly due to multiple scattering within the tissue, phase-front distortion by index variations, and absorption [15]. It was recognized already in the early days of OCT that among these the main limiting factor is scattering rather than absorption [16].

A Michelson interferometer incorporating a single linear detector measures the first-order coherence of light, $g^{(1)}(\tau)$, namely the autocorrelation of the electric field. Such an interferometer has been used for almost a century to measure the diameter of stars [17]; however, its utility significantly suffers from atmospheric turbulence and instrumental fluctuations. During the late 1950s, a dramatic solution to this problem was offered by Hanbury-Brown and Twiss (HBT) [18], who replaced the single detector by two detectors with their electrical outputs multiplied, measuring the second-order coherence of the light source, $g^{(2)}(\tau)$, namely the autocorrelation of its intensity. The demonstration that such a measurement is unaffected by phase variations while carrying the desired information generated a great stir in the physics community and was one of the initiations of the field of quantum optics. However, the evolution from the Michelson interferometer to the HBT setup cannot be simply traced in the field of OCT because the electronic multiplication at the output of the detectors limits the time resolution to the picosecond range, much too slow to achieve reasonable imaging resolution. This time-response limitation can be overcome if entangled photons are used, in a field usually referred to as quantum OCT, based on the Hong–Ou–Mandel effect [19]. This technique results in dispersion cancellation and therefore improved resolution; however, the efficient generation and manipulation of entangled photons is still rather challenging for practical applications. Classical analogies of this technique using chirped-pulse interferometry [20] or phase-matched sum-frequency generation [21] also suffer from relatively high complexity. Recently, a method for ultrafast characterization of the second-order coherence of light sources was presented based on the nearly instantaneous intensity multiplication of two-photon absorption (TPA) [Fig. 1(a)] in a photomultiplier tube (PMT) [22]. The ultrabroad bandwidth of TPA and the high sensitivity of the PMT to two-photon detection [23] enabled the measurement of the short coherence times of chaotic sources such as halogen lamps. This method was also recently exploited for the measurement of extra-bunching [24] and for a demonstration of interference between two chaotic sources [25].

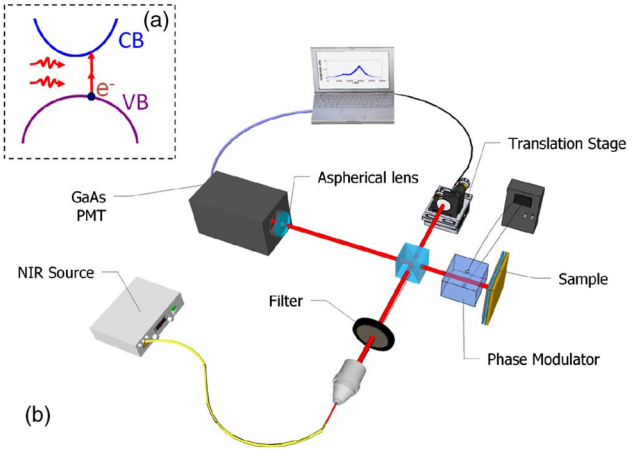

Fig. 1. (Color online) (a) Schematics of TPA in a semiconductor direct-bandgap material (CB, conduction band; VB, valence band). (b) SO-OCT setup: a chaotic NIR source enters a Michelson interferometer through a $\lambda > 1$ μm filter and is detected at the output by TPA in a GaAs PMT. A phase modulator located before the sample generates temporal phase variations.

Here we show the unique characteristics of a time-domain OCT system based on a two-photon detector [Fig. 1(b)], which we term second-order OCT (SO-OCT). These characteristics include the capability to measure through media with spatially variant phase, robustness to multiple scattering inside the desired sample volume, robustness to temporal turbulence or subwavelength motion of the sample, and inherent ability to extract anisotropic-sample information. We show that while our method is insensitive both to spatial and temporal turbulence, the output of the current method of OCT, based on $g^{(1)}(\tau)$ measurement, is completely destroyed under such conditions. Because biological tissues are known to have refractive-index variations with a turbulent nature [26], this has dramatic implications on the limited depth of conventional OCT.

2. RESULTS

A. Limitations of Standard OCT

The fundamental concept behind conventional OCT is that the first-order temporal coherence function of a broadband optical source, implemented either directly by broadband emission or using a swept laser source, is very narrow and localized around the symmetry point of the interferometer. For a sample with multiple reflectors, a symmetry point exists for each reflector, resulting in a superposition of temporal coherence functions localized around each reflector location. The amplitude of each of these functions is proportional to the value of the corresponding reflectivity. Assuming no polarization changes, no lateral spatial variations, and no temporal phase variations while propagating through the sample, the normalized output signal as a function of the time difference between the arms of the interferometer, τ (which can be translated to distance using the speed of light in vacuum), is

$$S^{(1)}(\tau) = C_1 + \sum_k a_k g^{(1)}(\tau - t_k), \tag{1}$$

where $C_1 = (1/2)(1 + \sum_k \sum_l a_k a_l g^{(1)}(t_k - t_l))$ is a background term independent of τ, a_k is the magnitude of the reflection coefficient of the kth reflector, t_k is the time-domain location of the kth reflector with respect to the symmetry point of the interferometer, and $g^{(1)}(\tau)$ is the (real) first-order coherence function of the light source, $g^{(1)}(\tau) = \mathrm{Re}\{(\langle E^*(t)E(t+\tau)\rangle)/(\langle E^*(t)E(t)\rangle)\}$, with $E(t)$ being the electric field at time t. For a chaotic source with Lorentzian line shape, for example, $g^{(1)}(\tau) = \exp[-(|\tau|/\tau_c)]\cos(\omega_0\tau)$, where τ_c is the coherence time of the source and ω_0 is the optical carrier frequency [Fig. 2(a)]. The interferogram in Eq. (1) presents a scan as a function of depth in OCT, which is usually referred to as "A-scan." The "localization" of the coherence function determines the resolution and is dictated by the coherence time of the source. The profile of the refractive index within the medium is encoded in the last term of Eq. (1),

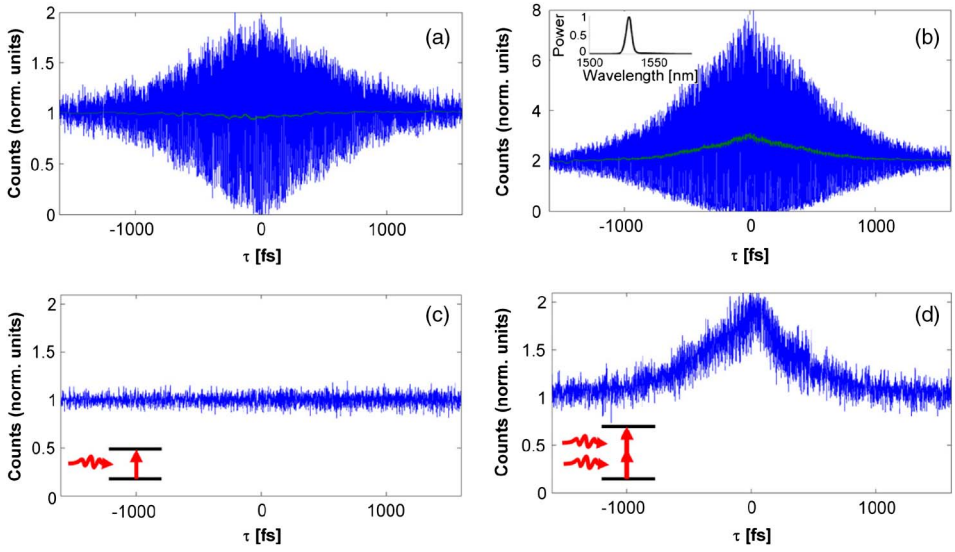

Fig. 2. (Color online) (a) First-order OCT measurement (blue) of a single reflector resulting in a high-frequency carrier multiplied by an exponentially decaying envelope, in addition to a constant background (green). (b) SO-OCT measurement of a single reflector resulting in frequency content around DC (green) in addition to high-frequency terms. The inset is the spectrum of the source. (c) Standard first-order OCT through temporally variant phase. The inset is a schematic of one-photon absorption. (d) SO-OCT through temporally variant phase. The inset is a schematic of TPA.

which is modulated by the carrier frequency, ω_0. Therefore, either envelope detection or demodulation is typically used to extract the tomographic information.

In practice, because the imaged tissues are optically dense, they do not conform to this simplified model of a collection of flat specular reflectors. Different ingredients of soft tissues including protein macromolecules and a gelatinous matrix of collagen and elastin fibers packed with cells, blood vessels, nerves, and numerous other structures, result in inhomogeneities in the refractive index with dimensions ranging from less than 100 nm to more than several millimeters [15]. Moreover, multiple scattering results in varying phase of the photons collected from the sample. This leads to a spatially variant phase of the image of the sample on the detector. Furthermore, subwavelength sample motion or temporal turbulence of the medium between the sample and the detector, such as bloodflow in cardiovascular applications [27], result in phase variations as a function of time within the integration time of the detector. Taking these effects into account, even for a sample consisting of perfect reflectors, the output of the detector from Eq. (1) is modified to

$$\tilde{S}^{(1)}(\tau) = \iint_{\mathrm{A}} \int_{0}^{T} S^{(1)}(\tau - \Delta\tau(x,y,t))\mathrm{d}x\mathrm{d}y\mathrm{d}t, \tag{2}$$

where $\omega_0\Delta\tau(x,y,t)$ is the phase variation at time t and location (x,y) within the beam's spot on the detector. For a given spatiotemporal distribution of $\Delta\tau(x,y,t)$, due to the oscillatory nature of $S^{(1)}(\tau)$, the larger the beam's cross section A or the integration time T are, the larger is the probability that $\tilde{S}^{(1)}(\tau)$ is strongly attenuated. If, for example, A and T are large and $\omega_0\Delta\tau$ varies uniformly over $[-\pi,\pi]$, due to either temporal or spatial fluctuations, then the signal almost completely vanishes [the last term in Eq. (1)]. Specifically, in this case $\tilde{S}^{(1)}(\tau) \approx C_1$ so that no information about the reflector locations is present in the measured signal. Thus, the phase fluctuations act as a low-pass filter in the interferogram domain.

High-speed acquisition can mitigate the effect of temporal phase variations at the expense of reduced signal-to-noise ratio (SNR). This is the case, for example, in cardiovascular imaging, where the velocity of the heart motion can be as high as 100 mm/s [28], implying that a phase change of 2π can occur during ~10 μs. Imaging to a small spot on the detector, however, does not mitigate the effect of spatial phase variations because the variations in phase are maintained, only on a smaller scale.

B. Unique Characteristics of SO-OCT

In contrast to a regular one-photon detector, a two-photon detector measures the second-order coherence of the impinging light, namely its intensity–intensity correlation, $g^{(2)}(\tau) = \langle I(t)I(t+\tau)\rangle/\langle I(t)\rangle^2$. This information is located around DC in the frequency content of the interferogram, which also contains contents around ω_0 and around $2\omega_0$ [22] [Fig. 2(b)]. While spatial and temporal integration, as in Eq. (2), attenuate the high-frequency terms due to subwavelength variations in $\Delta\tau(x,y,t)$, they hardly affect the content around DC. This allows extracting information on the reflectors' locations in a manner that is insensitive to spatial and temporal phase fluctuations. This stems from the fact that while interference fringes appear in the field correlation function they are absent in the intensity correlation function.

In order to obtain "localized" functions, as in the first-order case, either pulsed or bunched sources must be used. Here we treat a chaotic source in which the photons are bunched, leading to an enhanced correlation around the symmetry point of the interferometer. For a chaotic light source, $S^{(2)}(\tau)$ takes on a particularly convenient form. Its low-frequency (around DC) term is given by (see Appendix A)

$$\begin{aligned} S^{(2)}_{\mathrm{LF}}(\tau) = C_2 &+ \sum_k a_k^2 \exp\left[-\frac{2|\tau - t_k|}{\tau_c}\right] \\ &+ \sum_k \sum_{l\neq k} a_k a_l \cos(\omega_0(t_k - t_l)) \\ &\times \exp\left[-\frac{|\tau - t_k| + |\tau - t_l|}{\tau_c}\right], \end{aligned} \tag{3}$$

where $C_2 = C_1^2$ is a background level. For well-separated reflectors, namely for $|t_k - t_l| \gg \tau_c$, the last term vanishes so that the scan comprises a combination of shifted second-order coherence functions, in our case $g^{(2)}(\tau) = 1 + \exp[-(2|\tau|/\tau_c)]$, at the reflectors' locations. The low-frequency term of $S^{(2)}(\tau)$ is only affected by phase variations that are on the order of the coherence time and not on the order of the optical time period, and therefore for subwavelength variations $\tilde{S}^{(2)}(\tau) = \iint_A \int_0^T S^{(2)}(\tau - \Delta\tau(x,y,t))\mathrm{d}x\mathrm{d}y\mathrm{d}t \cong S^{(2)}_{\mathrm{LF}}$. It is interesting to note that $g^{(2)}(\tau)$ has half the decay-time of $g^{(1)}(\tau)$, which presumably indicates of improved resolution, as theoretically claimed in [29]. However, this analysis does not take into account the last term in Eq. (3), which becomes significant when measuring two adjacent reflectors.

1. Robustness to Spatiotemporal Turbulence

As a first demonstration of the robustness of our system to temporal turbulence, we have inserted a phase modulator in the sample arm of the interferometer modulated by a triangular wave in the range $[-\pi,\pi]$ within the integration time of the detector, with the sample being a perfect reflector. We used a chaotic light source implemented by amplified spontaneous emission around a wavelength of 1.53 μm [Fig. 2(b), inset] from an Er^{3+}-doped fiber amplifier (EDFA) with a coherence time of $\tau_{c,L} = 1170$ fs. Under these conditions, and using linear detection by an InGaAs detector, as in conventional OCT, the measurement yields a flat background [Fig. 2(c)] with no indication of the reflector's location. Replacing the detector with a GaAs PMT, which measures the signal by two-photon detections only, the existence of the reflector is clearly revealed, while the phase variations only attenuate the ω_0 and $2\omega_0$ components of the interferogram [Fig. 2(d)]. Because the information located around ω_0 in the second-order interferogram is identical to that of a first-order measurement, the fact that no fringes are observed in the second-order experiment would have sufficed by itself to conclude that the first-order signal (namely the regular OCT signal) would be completely erased under the same conditions. It should be pointed out that the fringe erasure is by itself a unique feature of SO-OCT, as deliberate phase variations may be added to the system, resulting in an interferogram with a DC term only. Such an interferogram can be

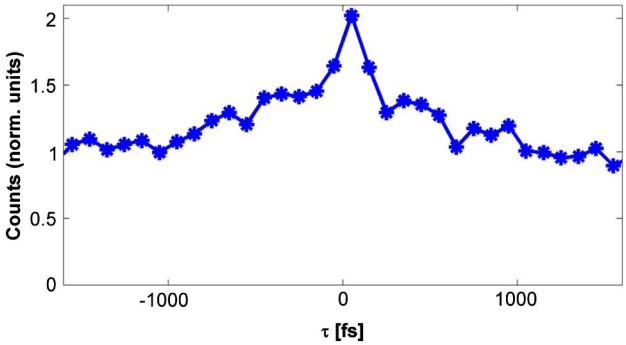

Fig. 3. (Color online) Sparsely sampled interferogram measured through temporally variant phase. The deliberate turbulence erases the high frequencies of the interferogram, enabling an ultralow sampling rate.

sampled at much lower sampling rates (Fig. 3) resulting in a significant increase in scan speed. Assuming that an integration time of 10 μs gives a sufficient SNR and that there are, for example, 10 optical cycles within the coherence length; because the SO-OCT signal is located around DC, the mirror movement can be at large steps of ~10 times the wavelength, therefore enabling a scan of 1 mm at ~1 ms. Taking into account the unique structure of the signal, one may employ advanced sub-Nyquist sampling methods, allowing even further reduction in sampling rates [30].

In order to demonstrate the tolerance of SO-OCT to spatial phase variations along the cross section of the beam, the perfect reflector was replaced with a phase spatial light modulator (SLM) incorporating a reflector at its back side. A random picture of phases from 0 to 2π was generated on the SLM, resulting again in a significant decrease in the visibility of the fringes while retaining the shape of $g^{(2)}(\tau)$ of the signal (Fig. 4).

It should be noted that although EDFAs are being used throughout the measurements to generate truly chaotic light, sources that are more popular in OCT applications, like superluminescent diodes (SLDs), can also be used, resulting in a slightly reduced amplitude of $g^{(2)}(0)$ to below 2. Moreover, the bandwidth of the chaotic source can be increased by combining several chaotic sources, similar to techniques used in standard OCT [31] with unique characteristics analyzed in [25]. This leads to a shorter coherence time and therefore a better resolution.

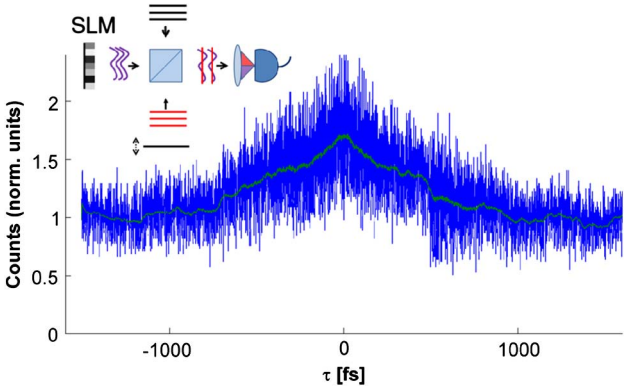

Fig. 4. (Color online) SO-OCT through spatially variant phase implemented using a phase-only SLM. The inset is a schematic of the setup.

C. Tolerance to Polarization Rotation

Another drawback of first-order interference is that the two fields involved must have a common polarization in order to interfere. Therefore, any polarization rotation in one arm of the interferometer with respect to the other arm reduces the visibility of the field–field interference fringes, and perpendicular polarizations result in a complete erasure of the signal. In order to be able to perform first-order imaging efficiently through anisotropic media, which changes the polarization of the reflected light, complex settings must be employed. These include the use of polarized light [32] or of dual-detector PS-OCT, which measures the two perpendicular polarizations simultaneously [33]. Intensity–intensity interference, on the other hand, exists even for perpendicular polarizations and is almost insensitive to the photons' polarization in bulk detectors [34]. At the same time, the fringes at ω_0, and $2\omega_0$ from the second-order interference are affected, and therefore the information about the amount of anisotropy of the sample is inherently encoded in the visibility factor of the measured interferogram. Because the matrix element of a two-photon transition is the square of the scalar product between two vector fields [35], it can be easily verified that the Fourier contents of the interferogram around ω_0 and around $2\omega_0$ are multiplied, respectively, by $\cos\theta$ and $\cos^2\theta$, where θ is the angle between the polarization of the fields. The $g^{(2)}(\tau)$ term around DC remains unaffected, as it is the result of a scalar product between the field in each of the arms with itself. To demonstrate this effect we have inserted a $\lambda/4$ waveplate into the sample arm of the interferometer, leading to a significant reduction in the fringes' visibility while maintaining the low-frequency term given by Eq. (3) (Fig. 5). The fringes do not vanish completely because the waveplate does not rotate the entire spectral width of the source.

D. Sensitivity of SO-OCT

Because TPA stems from a second-order term in perturbation theory, its matrix element is several orders of magnitude smaller than that of the first-order term. However, the TPA transition rate is proportional to the square of the intensity, implying that its efficiency can, in principle, be dramatically enhanced to values approaching those of the first order. The intensity can be increased either by focusing to a small spot on the detector or by increasing the intensity of the source. The

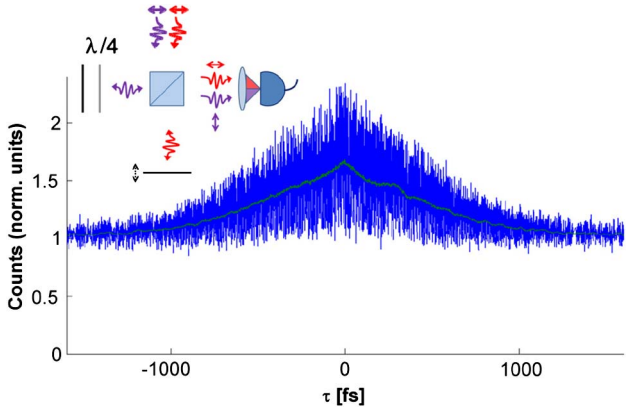

Fig. 5. (Color online) SO-OCT measurement of a single reflector with a $\lambda/4$ waveplate located before the sample, generating nearly orthogonal polarizations and therefore reduced visibility of the fringes only. The inset is a schematic of the setup.

detector used in our experiments can detect CW light levels down to ~1 μW without using lock-in schemes and without optimizing it for two-photon detections [the detector is designated for visible wavelengths, therefore the antireflection coating is not suitable for near infrared (NIR). Moreover, the distance between its front glass and the active layer is too large to reach a diffraction-limited spot on the detector, and the layer thickness is not optimized for long nonlinear interaction]. For biological samples, pulsed sources may be advantageous because current SLD emission results in a power of nanowatts arriving to the detector. While for regular OCT pulsed sources are attractive, as they give improved resolutions, in SO-OCT they also lead to a significant improvement in detection probability. Considering typical parameters of a suitable pulsed laser (e.g., FemtoFiber pro UCP, TOPTICA): pulse width <25 fs, mean power >30 mW, bandwidth 980–1400 nm, at a frequency of 80 MHz, we get a peak-intensity-to-average-intensity ratio of $I_{\text{Peak}}/I_{\text{Average}} = 5 \cdot 10^6$. TPA is quadratic in intensity, meaning that, by replacing a 30 mW continuous source with this femtosecond source, the SNR is improved by 11 orders of magnitude. Of course, a system based on ultrashort pulses should be carefully engineered in terms of dispersion to maintain the high resolution.

3. DISCUSSION

The main factors responsible for the limited imaging depth in first-order OCT are absorption, weak reflection, multiple backscattering, and multiple forward scattering. In most biological tissues, the latter two are the most dominant factors [36]. Here we focus on tissues with a dominant multiple-scattering mechanism. To isolate the effect of multiple forward scattering on the depth limit of OCT, we assume here that $\Delta\tau(x, y, t)$ in Eq. (2) is not a function of t, so that the temporal integration can be disregarded. Furthermore, we consider a refractive index varying spatially in the medium as a stationary random field. In this case, if the radius of the cross section A of the beam is much larger than the characteristic length of refractive-index variations, then the spatial integration in Eq. (2) can be replaced by a mean over realizations, namely $\tilde{S}^{(1)}(\tau) = \langle S^{(1)}(\tau - \Delta\tau)\rangle = \int S^{(1)}(\tau - \eta) f_{\Delta\tau}(\eta) \mathrm{d}\eta$, where $f_{\Delta\tau}$ is the probability density function of $\Delta\tau$. Thus, $\tilde{S}^{(1)}(\tau)$ is the result of convolving $S^{(1)}(\tau)$ with $f_{\Delta\tau}$. As the frequency contents of the former are concentrated around ω_0 and the latter is of a low-pass nature, this results in effective attenuation (Fig. 6, inset).

It has been shown in [26] that spatial correlations in the refractive index within biological tissues can be described by the Matérn model [37], with characteristic variation length L_0 on the order of 4–10 μm. Assuming that the refractive index fluctuation δn is a Gaussian random field, if a perfect reflector is placed at a distance of $L/2$ below the surface, then $f_{\Delta\tau}(\eta)$ is a Gaussian function with mean zero and variance $\langle\Delta\tau^2\rangle = (2L_0\langle\delta n^2\rangle/c)(L - L_0(1 - e^{-(L/L_0)}))$, where c is the speed of light and $\langle\delta n^2\rangle$ is the fluctuations' variance. In this case, using a chaotic light source with Gaussian broadening in a conventional OCT (first order) results in an attenuation of the peak of the interferogram's envelope by a factor of (see Appendix)

$$\alpha_1 = \frac{\tau_c}{\tilde{\tau}_c} \exp\left\{-\frac{\tau_c^2 \omega_0^2 \langle\Delta\tau^2\rangle}{2\tilde{\tau}_c^2}\right\}, \tag{4}$$

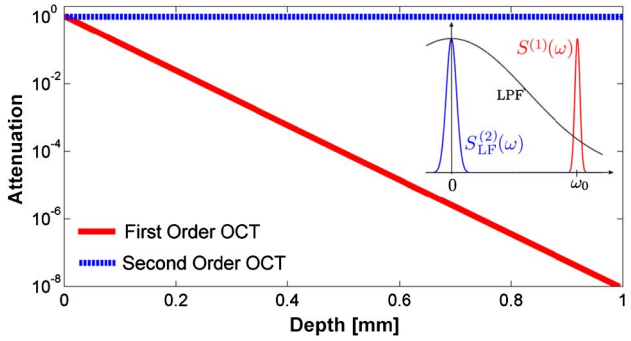

Fig. 6. (Color online) Value of the peak of the interferogram's envelope in first- and second-order OCT for imaging through turbid media as a function of depth [Eqs. (4) and (5)] for $L_0 = 4$ μm, $\langle\delta n^2\rangle = 0.01^2$, and a source of wavelength 1.3 μm and coherence time $\tau_c = 100$ fs. The inset visualizes the frequency content of the two modalities along with the frequency response of the low-pass filter (LPF) caused by the phase variations.

where $\tilde{\tau}_c^2 = \tau_c^2 + \pi\langle\Delta\tau^2\rangle$. It can be seen that for phase shifts on the order of the optical wavelength or larger, the term $\omega_0^2\langle\Delta\tau^2\rangle$ is dominant and the effective attenuation is significant. By contrast, the attenuation factor for the low-frequency (near-DC) term of the SO-OCT measurement in the same setting is

$$\alpha_2 = \frac{\tau_c}{\tau_c + 2\pi\langle\Delta\tau^2\rangle}. \tag{5}$$

This factor becomes significant only when the phase variations are on the order of the coherence time of the source, which is typically much larger than the optical wavelength. In fact, Eqs. (4) and (5) reveal that the signal in conventional OCT decays roughly exponentially as a function of the depth L whereas the signal in SO-OCT decays roughly as $1/L$. This has a dramatic implication on the attainable improvement in SNR by increasing integration time. Figure 6 illustrates this dramatic difference by depicting the decay as a function of imaging depth for first-order OCT and SO-OCT with parameters typical to biological tissues [26,38]. Specifically, the parameters of the Matérn model used in this simulation roughly match those measured in [26] for human upper dermis (see Appendix), and the refractive index fluctuation variance, $\langle\delta n^2\rangle$, is 0.01^2, in accordance with the values reported in [38]. Of course, optical absorption within the tissue limits the penetration depth of any type of optical imaging modality; however, the absorption length in most tissues is at least an order of magnitude larger than the scattering length [39]. Therefore, reducing the sensitivity to scattering results in significant improvement in imaging depth.

It should be noted that Eq. (2) assumes full-field imaging of the sample on the detector, while OCT is generally performed with setups consisting of single-mode fibers. When using single-mode fibers mostly "ballistic photons," photons that traveled through the turbid medium without being scattered, are extracted. This, however, means that only a small portion of the energy reflected from the sample is used, and the probability for such photons to arrive at the detector decreases significantly with increased imaging depth. The same issue arises in free-space systems if the detector is located

at the focal plane because light from the reference arm is focused to a small spot on the detector, overlapping only the low-spatial-frequency part (negligible transverse wavevector) of light arriving from the sample. Our method, on the other hand, also utilizes the information from the scattered photons, as long as their scattering variation is less than the coherence length. Such photons are available from deeper layers of the sample.

It is interesting to note that from a quantum-mechanical perspective, the robustness of our method is attributed to the indistinguishability between the two paths the photon pair may take in the interferometer before being absorbed by TPA, similar to the temporal-turbulence robustness of ghost-imaging techniques based on HBT setups [40]. The increased signal around a symmetry point results from a constructive interference of two indistinguishable Feynman alternatives for detection: (1) photon 1 went through the turbulence and reflected from the sample, while photon 2 went to the reference mirror and (2) photon 2 went through the turbulence, while photon 1 went to the reference mirror, so that the phase shifts are canceled in pairs. SO-OCT can, in fact, be viewed as the temporal equivalent of ghost imaging, with an object of slits [41], for example, replaced with a sequence of reflectors, and the electronic multiplication of the two detectors replaced by an optical TPA multiplication.

In conclusion, second-order coherence measurements have unique characteristics leading to robustness to both temporal as well as spatial turbulence. Utilizing these characteristics in OCT measurements based on the ultrafast optical multiplication of TPA enables high-resolution depth imaging with depth limited by the absorption coefficient of the medium rather than its scattering coefficient. This is specifically significant in highly scattering tissues such as human skin. Other striking features arise, including the possibility for sparse sampling and the extraction of structural information. This opens up new possibilities in the field of optical imaging in biological tissues and in other applications beyond biomedicine, such as, metrology, material characterization, and volumetric data storage.

APPENDIX A

1. Derivation of First- and Second-Order OCT Signals

The first-order OCT signal, corresponding to a discrete set of reflectors, is given by $S^{(1)}(\tau) = \langle |E(t-\tau) + \sum_k a_k E(t-t_k)|^2 \rangle$. Written explicitly, this expression leads to Eq. (1). For SO-OCT, $S^{(2)}(\tau) = \langle |E(t-\tau) + \Sigma_k a_k E(t-t_k)|^4 \rangle$, which can be calculated explicitly for chaotic light, leading to Eq. (3). However, because chaotic light comprises numerous contributions of independent emissions, its electric field is a Gaussian random process. The fourth-order moment of a zero-mean Gaussian variable equals 3 times its squared second-order moment, so that the SO-OCT measurement can be simply expressed as

$$S^{(2)}(\tau) = \left\langle \left| E(t-\tau) + \sum_k a_k E(t-t_k) \right|^4 \right\rangle = 3\left\langle \left| E(t-\tau) + \sum_k a_k E(t-t_k) \right|^2 \right\rangle^2 = 3(S^{(1)}(\tau))^2. \quad \text{(A1)}$$

Substituting Eq. (1), and separating the low-frequency terms, this expression leads to Eq. (3).

2. Second-Order Coherence Setup

The chaotic radiation sources were implemented by an EDFA with 17 dBm maximal output at fixed gain (manufactured by RED-C). The output power was controlled using the variable gain and using constant fiber attenuators, attaining a level of ~200 μW at the detector. The optical radiation was coupled from the fibers to free space using a collimator lens and was filtered by a 300 μm thick silicon layer, absorbing any undesired low-wavelength emission that may be detected by one-photon absorption in the detector. The wide spread of the collimated beam renders any nonlinear processes in the silicon negligible. Subsequently, the optical radiation was inserted into a computer-controlled Michelson interferometer incorporating a broadband beam splitter (1100–1600 nm) and a translation stage with 50 nm resolution (Thorlabs DRV001). A GaAs PMT detector (Hamamatsu H7421-50) was used for efficient TPA at the wavelength range of 1500–1600 nm. The Michelson interferometer and the detector were placed inside a light shield to reduce background detections. Because TPA probability in the detector is inversely proportional to the spot area, the signal was imaged on the PMT detector by an aspherical lens with focal length of $f = 25$ mm and numerical aperture of 0.5.

3. First-Order Coherence Setup

The output from the Michelson interferometer was attenuated, coupled to a fiber, and connected to an InGaAs single-photon detector (Princeton Lightwave).

4. Temporal Phase Modulation

An electro-optic phase modulator for wavelength 1250–1650 nm (Thorlabs EO-PM-NR-C3) was placed before the sample, modulated by a triangular voltage wave at a frequency of 10 kHz, resulting in 10 cycles of phase variation from 0 to 2π within the integration time of the detector. The optical input was linearly polarized and aligned with the extraordinary axis of the modulator crystal, resulting in a pure phase shift with no change in the state of polarization.

5. Spatial Phase Modulation

The sample was replaced with a phase-only microdisplay (HOLOEYE HED 6010 TELCO) optimized for 1550 nm with a resolution of 1920×1080 pixels and pixel pitch of 8 μm. A random bitmap image was used generating ~2000 random-phase elements within the cross section of the beam.

6. Derivation of Attenuation Factor

To analyze the attenuation factor, we rely on the fact that the refractive index is given by $n(x,y,z) = \bar{n} + \delta n(x,y,z)$, where $\delta n(x,y,z)$ is an isotropic Gaussian random field. It was shown in [26] that in biological tissues, the spatial spectrum corresponding to a two-dimensional slice $\delta n(x,y,0)$ is of the form

$$\frac{4\pi \langle \delta n^2 \rangle L_0 (m-1)}{(1 + L_0^2 \|\omega\|^2)^m}, \quad \text{(A2)}$$

where $\omega = (\omega_x, \omega_y)$ denotes spatial frequency, $\langle \delta n^2 \rangle$ is the field's variance and, L_0 is a scale parameter, often referred

to as the outer scale of the field. The value of m was found to lie between 1.28 and 1.43 in most tissues. For simplicity, we focus on the value $m = 1.5$, which is close to that measured in [26] for human upper dermis ($m = 1.43$). The corresponding autocorrelation function is $R_{\delta n}(d) = \langle \delta n^2 \rangle e^{-(d/L_0)}$, where d denotes displacement length. In this situation, if a perfect reflector is placed at a distance of $L/2$ below the surface, then $f_{\Delta\tau}(\eta)$ is a Gaussian function with mean zero and variance

$$\begin{aligned}\langle \Delta\tau^2 \rangle &= \left\langle \left(\frac{1}{c} \int_0^L \delta n(0,0,z) \mathrm{d}z \right)^2 \right\rangle \\ &= \frac{1}{c^2} \int_0^L \int_0^L R_{\delta n}(z_1 - z_2) \mathrm{d}z_1 \mathrm{d}z_2 \\ &= \frac{2L_0 \langle \delta n^2 \rangle}{c} \left(L - L_0 \left(1 - e^{-\frac{L}{L_0}} \right) \right), \end{aligned} \tag{A3}$$

where c is the speed of light.

When using a chaotic source with Gaussian broadening, $g^{(1)}(\tau) = \exp[-\pi\tau^2/2\tau_c^2]\cos(\omega_0\tau)$, so that the convolution between $f_{\Delta\tau}(\eta)$ and $g^{(1)}(\tau)$ can be calculated in closed form, yielding

$$\tilde{S}^{(1)}(\tau) = \alpha \exp\left[-\frac{\pi\tau^2}{2\tilde{\tau}_{c,1}^2} \right] \cos(\tilde{\omega}_0 \tau). \tag{A4}$$

Here, $\tilde{\tau}_{c,1}^2 = \tau_c^2 + \pi\langle \Delta\tau^2 \rangle$, $\tilde{\omega}_0 = (\tau_c^2/\tilde{\tau}_c^2)\omega_0$, and the attenuation factor α_1 is given by

$$\alpha_1 = \frac{\tau_c}{\tilde{\tau}_{c,1}} \exp\left\{ -\frac{\tau_c^2 \omega_0 \langle \Delta\tau^2 \rangle}{2\tilde{\tau}_{c,1}^2} \right\}. \tag{A5}$$

For the same setting, $g^{(2)}(\tau) = 1 + \exp[-(\pi\tau^2/\tau_c^2)]$, and similar computation reveals that the low-frequency term of the SO-OCT becomes

$$\tilde{S}^{(2)}(\tau) = 1 + \alpha_2 \exp\left[-\frac{\pi\tau^2}{\tilde{\tau}_{c,2}^2} \right], \tag{A6}$$

with $\tilde{\tau}_{c,2}^2 = \tau_c^2 + 2\pi\langle \Delta\tau^2 \rangle$ and attenuation factor $\alpha_2 = \tau_c/\tilde{\tau}_{c,2}$.

The attenuation factors α_1 and α_2 are plotted in Fig. 6 as a function of penetration depth for $m = 1.5$ and $L_0 = 4$ μm, which are values close those measured in [26] for human upper dermis ($m = 1.43$ and $L_0 = 4$ μm), and for $\langle \delta n^2 \rangle = 0.01^2$, which is within the range $[0.007^2, 0.022^2]$ reported in [38]. In this simulation, the chaotic source is of wavelength 1.3 μm and coherence time $\tau_c = 100\,fs$.

ACKNOWLEDGMENT

This research was partially supported by the Israel Science Foundation (ISF) grant number 68108 and by the Focal Technology Area on Nanophotonics for Detection. A. N. is supported by the Adams Fellowship Program of the Israel Academy of Sciences and Humanities.

REFERENCES

1. W. Drexler and J. G. Fujimoto, eds., *Optical Coherence Tomography: Technology and Applications* (Springer, 2008).
2. R. C. Youngquist, S. Carr, and D. E. N. Davies, "Optical coherence-domain reflectometry: a new optical evaluation technique," Opt. Lett. **12**, 158–160 (1987).
3. H. H. Gilgen, R. P. Novak, R. P. Salathé, W. Hodel, and P. Beaud, "Submillimeter optical reflectometry," J. Lightwave Technol. **7**, 1225–1233 (1989).
4. D. Huang, E. A. Swanson, C. P. Lin, J. S. Schuman, W. G. Stinson, W. Chang, M. R. Hee, T. Flotte, K. Gregory, C. Puliafato, and J. G. Fujimoto, "Optical coherence tomography," Science **254**, 1178–1181 (1991).
5. W. Geitzenauer, C. K. Hitzenberger, and U. M. Schmidt-Erfurth, "Retinal optical coherence tomography: past, present and future perspectives," Br. J. Ophthalmol. **95**, 171–177 (2011).
6. F. Prati, E. Regar, G. S. Mintz, E. Arbustini, C. Di Mario, I.-K. Jang, T. Akasaka, M. Costa, G. Guagliumi, E. Grube, Y. Ozaki, F. Pinto, and P. W. J. Serruys, "Expert review document on methodology, terminology and clinical applications of optical coherence tomography: physical principles, methodology of image acquisition and clinical application for assessment of coronary arteries and atherosclerosis," Eur. Heart J. **31**, 401–415 (2010).
7. L. Liu, J. A. Gardecki, S. K. Nadkarni, J. D. Toussaint, Y. Yagi, B. E. Bouma, and G. J. Tearney, "Imaging the subcellular structure of human coronary atherosclerosis using micro-optical coherence tomography," Nat. Med. **17**, 1010–1014 (2011).
8. M. C. Pierce, J. Strasswimmer, B. H. Park, B. Cense, and J. F. de Boer, "Advances in optical coherence tomography imaging for dermatology," J. Invest. Dermatol. **123**, 458–463 (2004).
9. D. Stifter, "Beyond biomedicine: a review of alternative applications and developments for optical coherence tomography," Appl. Phys. B **88**, 337–357 (2007).
10. A. F. Fercher, C. K. Hitzenberger, G. Kamp, and S. Y. El-Zaiat, "Measurements of intraocular distances by backscattering spectral interferometry," Opt. Commun. **117**, 43–48 (1995).
11. G. Hausler and M. W. Lindner, "Coherence radar and spectral radar—new tools for dermatological diagnosis," J. Biomed. Opt. **3**, 21–31 (1998).
12. M. E. Brezinski, *Optical Coherence Tomography: Principles and Applications* (Academic, 2006).
13. S. H. Yun, G. Tearney, J. de Boer, and B. Bouma, "Motion artifacts in optical coherence tomography with frequency-domain ranging," Opt. Express **12**, 2977–2998 (2004).
14. J. F. de Boer and T. E. Milner, "Review of polarization sensitive optical coherence tomography and Stokes vector determination," J. Biomed. Opt. **7**, 359–371 (2002).
15. J. M. Schmitt, "Optical coherence tomography (OCT): a review," IEEE J. Sel. Top. Quantum Electron. **5**, 1205–1215 (1999).
16. J. M. Schmitt, A. Knuttel, M. Yadlowsky, and M. A. Eckhaus, "Optical-coherence tomography of a dense tissue: statistics of attenuation and backscattering," Phys. Med. Biol. **39**, 1705–1720 (1994).
17. R. Loudon, *The Quantum Theory of Light*, 3rd ed. (Oxford University, 2000).
18. R. Hanbury-Brown and R. Q. Twiss, "A test of a new type of stellar interferometer on Sirius," Nature **177**, 1046–1048 (1956).
19. M. B. Nasr, B. E. A. Saleh, A. V. Sergienko, and M. C. Teich, "Demonstration of dispersion-canceled quantum-optical coherence tomography," Phys. Rev. Lett. **91**, 083601 (2003).
20. J. Lavoie, R. Kaltenbaek, and K. J. Resch, "Quantum-optical coherence tomography with classical light," Opt. Express **17**, 3818–3825 (2009).
21. A. Pe'er, Y. Bromberg, B. Dayan, Y. Silberberg, and A. A. Friesem, "Broadband sum-frequency generation as an efficient two-photon detector for optical tomography," Opt. Express **15**, 8760–8769 (2007).
22. F. Boitier, A. Godard, E. Rosencher, and C. Fabre, "Measuring photon bunching at ultrashort timescale by two-photon absorption in semiconductors," Nat. Phys. **5**, 267–270 (2009).
23. J. M. Roth, T. E. Murphy, and C. Xu, "Ultrasensitive and high-dynamic-range two-photon absorption in a GaAs photomultiplier tube," Opt. Lett. **27**, 2076–2078 (2002).
24. F. Boitier, A. Godard, N. Dubreuil, P. Delaye, C. Fabre, and E. Rosencher, "Photon extrabunching in ultrabright twin beams measured by two-photon counting in a semiconductor," Nat. Commun. **2**, 425 (2011).
25. A. Nevet, A. Hayat, P. Ginzburg, and M. Orenstein, "Indistinguishable photon pairs from independent true chaotic sources," Phys. Rev. Lett. **107**, 253601 (2011).

26. J. M. Schmitt and G. Kumar, "Turbulent nature of refractive-index variations in biological tissue," Opt. Lett. **21**, 1310–1312 (1996).
27. T. Kubo and T. Asakura, "Optical coherence tomography imaging: current status and future perspectives," Cardiovasc. Interv. Ther. **25**, 2–10 (2010).
28. S. M. Stengel, Y. Allemann, M. Zimmerli, E. Lipp, N. Kucher, P. Mohacsi, and C. Seiler, "Doppler tissue imaging for assessing left ventricular diastolic dysfunction in heart transplant rejection," Heart **86**, 432–437 (2001).
29. H. Lajunen, V. Torres-Company, J. Lancis, and A. T. Friberg, "Resolution-enhanced optical coherence tomography based on classical intensity interferometry," J. Opt. Soc. Am. A **26**, 1049–1054 (2009).
30. T. Michaeli and Y. C. Eldar, "Xampling at the rate of innovation," IEEE Trans. Signal Process. **60**, 1121–1133 (2012).
31. T. H. Ko, D. C. Adler, J. G. Fujimoto, D. Mamedov, V. Prokhorov, V. Shidlovski, and S. Yakubovich, "Ultrahigh resolution optical coherence tomography imaging with a broadband superluminescent diode light source," Opt. Express **12**, 2112–2119 (2004).
32. J. F. de Boer, T. E. Milner, M. J. C. van Gemert, and J. S. Nelson, "Two-dimensional birefringence imaging in biological tissue by polarization-sensitive optical coherence tomography," Opt. Lett. **22**, 934–936 (1997).
33. M. J. Everett, K. Schoenenberger, B. W. Colston, Jr., and L. B. Da Silva, "Birefringence characterization of biological tissue by use of optical coherence tomography," Opt. Lett. **23**, 228–230 (1998).
34. R. Salem and T. E. Murphy, "Polarization-insensitive cross correlation using two-photon absorption in a silicon photodiode," Opt. Lett. **29**, 1524–1526 (2004).
35. A. Hayat, P. Ginzburg, and M. Orenstein, "Observation of two-photon emission from semiconductors," Nat. Photonics **2**, 238–241 (2008).
36. J. M. Schmitt, S. H. Xiang, and K. M. Yung, "Speckle in optical coherence tomography," J. Biomed. Opt. **4**, 95–105 (1999).
37. M. S. Handcock and M. L. Stein, "A Bayesian analysis of kriging," Technometrics **35**, 403–410 (1993).
38. J. M. Schmitt, S. H. Xiang, and K. M. Yung, "Quantitatively characterizing fluctuations of dielectric susceptibility of tissue with Fourier domain optical coherence tomography," J. Opt. Soc. Am. A **27**, 2588–2592 (2010).
39. P. van der Zee, "Measurement and modelling of the optical properties of human tissue in the near infrared," Ph. D. dissertation (Department of Medical Physics and Bioengineering, University College London, 1993).
40. R. E. Meyers, K. S. Deacon, and Y. Shih, "Turbulence-free ghost imaging," Appl. Phys. Lett. **98**, 111115 (2011).
41. F. Ferri, D. Magatti, A. Gatti, M. Bache, E. Brambilla, and L. A. Lugiato, "High-resolution ghost image and ghost diffraction experiments with thermal light," Phys. Rev. Lett. **94**, 183602 (2005).